A Sparsity-Driven Approach for Joint SAR Imaging and Phase Error Correction

N. Özben Önhon, *Student Member, IEEE*, and Müjdat Çetin, *Member, IEEE*

Abstract—**Image formation algorithms in a variety of applications have explicit or implicit dependence on a mathematical model of the observation process. Inaccuracies in the observation model may cause various degradations and artifacts in the reconstructed images. The application of interest in this paper is synthetic aperture radar (SAR) imaging, which particularly suffers from motion-induced model errors. These types of errors result in phase errors in SAR data, which cause defocusing of the reconstructed images. Particularly focusing on imaging of fields that admit a sparse representation, we propose a sparsity-driven method for joint SAR imaging and phase error correction. Phase error correction is performed during the image formation process. The problem is set up as an optimization problem in a non-quadratic regularization-based framework. The method involves an iterative algorithm, where each iteration of which consists of consecutive steps of image formation and model error correction. Experimental results show the effectiveness of the approach for various types of phase errors, as well as the improvements that it provides over existing techniques for model error compensation in SAR.**

Index Terms—**Autofocus, phase errors, regularization, sparsity, synthetic aperture radar (SAR).**

I. INTRODUCTION

SYNTHETIC aperture radar (SAR) has recently been and continues to be a sensor of great interest in a variety of remote sensing applications, particularly because it overcomes certain limitations of other sensing modalities. First, SAR is an active sensor using its own illumination. To illuminate a ground patch of interest, the SAR sensor uses microwave signals that provide SAR with the capability of imaging day and night as well as in adverse weather conditions. Due to these features of SAR, SAR image formation has become an important research topic. The problem of SAR image formation is a typical example of inverse problems in imaging. The solution of inverse problems in imaging requires the use of a mathematical model of the observation process. However, such models often involve errors and uncertainties themselves. As a predominant example

in SAR imaging, motion-induced errors are reasons for model uncertainties that may cause undesired artifacts in the formed imagery. This type of errors causes phase errors in the SAR data, which result in defocusing of the reconstructed images [1]. Because of the defocusing effect of such errors, the techniques developed for removing phase errors are often called autofocus techniques.

Various studies have been presented on the SAR autofocus problem [2]–[17]. One of the most well-known techniques, i.e., phase gradient autofocus (PGA) [2], estimates phase errors using the data obtained by isolating many single defocused targets via center-shifting and windowing operations. It is based on the assumption that there is a single target at each range coordinate. Another well-known approach for autofocus is based on the optimization of a sharpness metric of the defocused image intensity [3]–[10]. These techniques aim to find the phase error estimate, which minimizes or maximizes a sharpness function of the conventionally reconstructed image. Commonly used metrics are entropy or square of the image intensity. Techniques such as map-drift autofocus [11] use subaperture data to estimate the phase errors. These techniques are suitable mostly for quadratic and slowly varying phase errors. A recently proposed autofocus technique, i.e., multichannel autofocus (MCA) [12], is based on a noniterative algorithm, which finds the focused image in terms of a basis formed from the defocused image, relying on a condition on the image support to obtain a unique solution. In particular, MCA estimates 1-D phase error functions by directly solving a set of linear equations obtained through an assumption that there are zero-reflectivity regions in the scene to be imaged. When this is not precisely satisfied, presence of a low-return region is exploited, and the phase error is estimated by minimizing the energy of the low-return region. When the desired conditions are satisfied, MCA performs very well. However, in scenarios involving low-quality data (e.g., due to low SNR) the performance of MCA degrades. A number of modifications to MCA have been proposed, including the incorporation of sharpness metric optimization into the framework [12], and the use of a semidefinite relaxation-based optimization procedure [17] for better phase error estimation performance.

One common aspect of all autofocus techniques referred to above is that they perform postprocessing, i.e., they use conventionally reconstructed (i.e., reconstructed by the polar-format algorithm [18], [19]) defocused images in the process of phase error estimation. However, our starting point is the observation that more advanced SAR image formation techniques have recently been developed. Of particular interest in this paper is the regularization-based SAR imaging (see, e.g., [20]–[22]),

which has been shown to offer certain improvements over conventional imaging. Regularization-based techniques can alleviate the problems in the case of incomplete data or sparse apertures. Moreover, they produce images with increased resolution, reduced sidelobes, and reduced speckle by incorporation of prior information about the features of interest and imposing various constraints (e.g., sparsity and smoothness) about the scene. However, existing regularization-based SAR imaging techniques rely on a perfect observation model and do not involve any mechanism for addressing any model uncertainties.

Motivated by these observations and considering scenes that admit sparse representation in some dictionary, we propose a sparsity-driven technique for joint SAR imaging and phase error correction by using a nonquadratic regularization-based framework. In the proposed sparsity-driven autofocus (SDA) method, phase errors are considered as model errors that are estimated and removed during image formation. The proposed method handles the problem as an optimization problem in which the cost function is composed of a data fidelity term (which exhibits dependence on the model parameters) and a regularization term, which is the l_1-norm of the field. For simplicity, we consider scenes that are spatially sparse; however, our approach can be applied to fields that are sparse in any given dictionary by using an l_1-norm penalty on the associated sparse representation coefficients. The cost function is iteratively minimized with respect to the field and the phase error using coordinate descent. In the first step of every iteration, the cost function is minimized with respect to the field, and in the second step, the phase error is estimated given the field estimate. The phase error estimate is used to update the model matrix, and the algorithm passes to the next iteration. To the best of our knowledge, this paper is first in the context of providing a solution to the problem of model errors in sparsity-driven image reconstruction.

Sharpness-based autofocus techniques [3]–[10] share certain aspects of our perspective, but our approach is fundamentally different. In particular, our approach also involves a certain type of sharpness metric about the field but inside of a cost function as a side constraint (regularization term) to a data fidelity term, which incorporates the system model and the data into the optimization problem for image formation. Hence, our approach imposes the sharpnesslike constraint during the process of image formation, rather than as postprocessing. This enables our technique to correct for artifacts in the scene due to model errors effectively, in an early stage of the image formation process. Furthermore, unlike existing sharpness-based autofocus techniques, our model error correction approach is coupled with an advanced sparsity-driven image formation technique that has the capability of producing high-resolution images with enhanced features, and as a result, our approach is not limited by the constraints of conventional SAR imaging. In fact, our approach benefits from a dual use of sparsity, i.e., both for model error correction (autofocusing) and for improved imaging. Finally, our framework is not limited to sharpness metrics on the scene but can be used in principle for model error correction in scenes that admit a sparse representation in any given dictionary.

We present results on synthetic scenes, as well as on two public data sets. Qualitative as well as quantitative analysis of the experimental results shows the effectiveness of the proposed method and the improvements it provides over existing methods in terms of both scene reconstruction and phase error estimation.

The rest of this paper is organized as follows. In Section II, the observation model for a SAR imaging system is described. In Section III, a general view of the phase errors and their effect on the SAR data are provided. In Section IV, the proposed method is described in detail, and in Section V, the experimental results are presented. We conclude this paper in Section VI and provide some technical details in the Appendix.

II. SAR OBSERVATION MODEL

In SAR systems, one of the most widely used signals in transmission is the chirp signal as follows:

$$s(t) = Re\left\{e^{\left[j(\omega_0 t + \alpha t^2)\right]}\right\}. \tag{1}$$

Here, ω_0 is the center frequency and 2α is the so-called chirp rate. For spotlight-mode SAR, which is the modality of interest in this paper, the relationship between the observed data $\bar{r}_m(t)$ at the mth aperture position, i.e., obtained after a preprocessing step, and the underlying field $F(x, y)$ is as follows:

$$\bar{r}_m(t) = \iint\limits_{x^2+y^2 \leq L^2} F(x,y)e^{-jU(x\cos\theta + y\sin\theta)}dxdy. \tag{2}$$

Here, L is the radius of the circular patch to be imaged, θ is the observation angle at the mth aperture position, and U has the following form:

$$U = \frac{2}{c}\left(\omega_0 + 2\alpha(t - \tau_0)\right). \tag{3}$$

Here, τ_0 is the round-trip propagation time (demodulation time). All of the returned signals from all observation angles constitute a patch from the 2-D spatial Fourier transform of the corresponding field. These data are called phase histories and lie on a polar grid in the 2-D frequency domain, as shown in Fig. 1. Let the 2-D discrete phase history data be denoted by a $K \times M$ matrix R. The column m of R, i.e., denoted by the $K \times 1$ vector $\bar{r}_m$, is obtained by sampling $\bar{r}_m(t)$ (the returned signal at cross-range position m), in fast time t (range direction) at K positions. In terms of this notation, the discrete observation model can be formulated as follows [20]:

$$\underbrace{\begin{bmatrix} \bar{r}_1 \\ \bar{r}_2 \\ \\ \\ \bar{r}_M \end{bmatrix}}_{r_{MK\times 1}} = \underbrace{\begin{bmatrix} \bar{C}_1 \\ \bar{C}_2 \\ \\ \\ \bar{C}_M \end{bmatrix}}_{C_{MK\times I}} f_{I\times 1}. \tag{4}$$

Here, the vector r of observed samples is obtained just by concatenating the columns of the 2-D phase history data R under each other. $\bar{C}_m$ and C are discretized approximations to the continuous observation kernel at the cross-range position m and for all cross-range positions, respectively. f is a vector representing the sampled and column-stacked version of the reflectivity image $F(x, y)$. Note that K and M are the total numbers of range and cross-range positions, respectively.
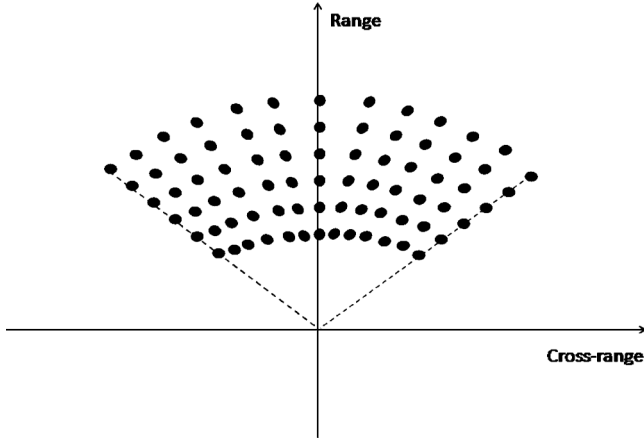
Fig. 1. Graphical representation of an annulus segment containing known samples of the phase history data in the 2-D frequency domain.

III. PHASE ERRORS

During the preprocessing of the SAR data (mentioned in Section II), the demodulation time τ_0 needs to be known. When this time is known imperfectly, the SAR data obtained after preprocessing contain phase errors. The inexact knowledge of the demodulation time occurs when the distance between the SAR sensor and the scene center cannot be determined perfectly due to SAR platform position uncertainties or when the signal has delay due to some atmospheric effects. Since uncertainties on, e.g., the position of the platform are constant over a signal received at one aperture position but are different at each aperture position, phase errors caused by such uncertainties vary only along the cross-range direction in the frequency domain. The implication of such an error in the image domain is the convolution of (each range line of) the image with a 1-D blurring kernel in the cross-range direction. Hence, such phase errors cause defocusing of the image in the cross-range direction. An example of SAR platform position uncertainties arises from errors in measuring the aircraft velocity. A constant error on aircraft velocity induces a quadratic phase error function in the data [1]. Usually, phase errors arising due to SAR platform position uncertainties are slowly varying (e.g., quadratic and polynomials) phase errors, whereas phase errors induced by propagation effects are much more irregular (e.g., random) phase errors [1]. While most phase errors encountered are 1-D cross-range-varying functions, it is possible to encounter both range and cross-range-varying 2-D phase errors as well. For instance, in low-frequency UWB SAR systems, severe propagation effects may appear through the ionosphere, including Faraday rotation, dispersion, and scintillation [23] that cause 2-D phase errors, defocusing the reconstructed image in both range and cross-range directions. Moreover, waveform errors such as frequency jitter from pulse to pulse, transmission-line reflections, and waveguide dispersion effects may cause defocus in both range and cross-range directions [18]. Two-dimensional phase errors can in principle be handled in two subcategories as separable and nonseparable

errors, but it is not common to encounter 2-D separable phase errors in practice.

For these three types of phase error functions, let us investigate the relationship between the phase-corrupted and error-free phase history data in terms of the observation model.

A. 2-D Nonseparable Phase Errors

In the presence of 2-D nonseparable phase errors, all sample points of the $K \times M$ phase history data are perturbed with different and potentially independent phase errors. Let $\Phi_{2\text{-D}-ns}$ be a 2-D nonseparable phase error function. The relationship between the phase-corrupted and error-free phase histories are as follows:

$$R_\epsilon(k,m) = R(k,m)e^{j\Phi_{2\text{-D}-ns}(k,m)}. \tag{5}$$

Here, R_ϵ denotes the phase-corrupted phase history data. To express this relationship in terms of the observation model, we first define the vector $\phi_{2\text{-D}-ns}$ as follows:

$$\phi_{2\text{-D}-ns} = [\phi_{2\text{-D}-ns}(1),\ \phi_{2\text{-D}-ns}(2),\dots,\phi_{2\text{-D}-ns}(S)]^T \tag{6}$$

which is created by concatenating the columns of the phase error matrix $\Phi_{2\text{-D}-ns}$ under each other. Here, S is the total number of data samples and equal to the product MK. Using the corresponding vector forms, the relationship in (5) becomes

$$r_\epsilon = D_{2\text{-D}-ns}r \tag{7}$$

where $D_{2\text{-D}-ns}$ is a diagonal matrix given as

$$D_{2\text{-D}-ns} = \text{diag}\left[e^{j\phi_{2\text{-D}-ns}(1)},\dots,e^{j\phi_{2\text{-D}-ns}(S)}\right]. \tag{8}$$

In terms of observation model matrices, the relationship in (7) is as follows:

$$C(\phi_{2\text{-D}-ns})f = D_{2\text{-D}-ns}Cf \tag{9}$$

where C is the initially assumed model matrix by the imaging system and $C(\phi_{2\text{-D}-ns})$ is the model matrix that takes the phase errors into account. The equations (7) and (9) can be expressed in the following form as well:

$$r_\epsilon(s) = e^{j\phi_{2\text{-D}-ns}(s)}r(s) \quad C_s(\phi_{2\text{-D}-ns})f = e^{j\phi_{2\text{-D}-ns}(s)}C_sf$$
$$\text{for} \quad s = 1,2,\dots,S. \tag{10}$$

Here, $r(s)$ denotes sth element of vector r and C_s denotes sth row of the model matrix C.

B. 2-D Separable Phase Errors

A 2-D separable phase error function is composed of range-varying and cross-range-varying 1-D phase error functions as follows:

$$\Phi_{2\text{-D}-s}(k,m) = \xi(k) + \gamma(m). \tag{11}$$

Here, ξ, representing the range-varying phase error, is a $K \times 1$ vector, and γ, representing the cross-range-varying phase error,

is an $M \times 1$ vector. The $S \times 1$ vector for 2-D separable phase errors $\phi_{2\text{-D}-s}$ is obtained by concatenating the columns of $\Phi_{2\text{-D}-s}$ as follows:

$$\phi_{2\text{-D}-s} = \left[\underbrace{\xi(1) + \gamma(1)}_{\phi_{2\text{-D}-s}(1)}, \ldots, \underbrace{\xi(K) + \gamma(1)}_{\phi_{2\text{-D}-s}(K)}, \underbrace{\xi(1) + \gamma(2)}_{\phi_{2\text{-D}-s}(K+1)}, \ldots, \right.$$
$$\left. \underbrace{\xi(1) + \gamma(M)}_{\phi_{2\text{-D}-s}((M-1)K+1)}, \ldots, \underbrace{\xi(K) + \gamma(M)}_{\phi_{2\text{-D}-s}(S)} \right]^T . \quad (12)$$

A 2-D separable phase error function affects the observation model matrix in the following manner:

$$r_\epsilon = D_{2\text{-D}-s} r \quad C(\phi_{2\text{-D}-s}) f = D_{2\text{-D}-s} C f. \quad (13)$$

Here, $D_{2\text{-D}-s}$ is a diagonal matrix given as

$$D_{2\text{-D}-s} = \text{diag}\left[e^{j\phi_{2\text{-D}-s}(1)}, e^{j\phi_{2\text{-D}-s}(2)}, \ldots, e^{j\phi_{2\text{-D}-s}(S)} \right]. \quad (14)$$

C. 1-D Phase Errors

We mentioned before that most encountered phase errors are only functions of the cross range. In other words, for a particular cross-range position, the phase error is same at all range positions. Let $\phi_{1\text{-D}}$ be the 1-D cross-range-varying phase error. $\phi_{1\text{-D}}$ is a vector of length M as follows:

$$\phi_{1\text{-D}} = [\phi_{1\text{-D}}(1), \ \phi_{1\text{-D}}(2), \ldots, \phi_{1\text{-D}}(M)]^T . \quad (15)$$

In the case of 1-D phase errors, the relationship between the error-free and the phase-corrupted data can be expressed as

$$r_\epsilon = D_{1\text{-D}} r \quad C(\phi_{1\text{-D}}) f = D_{1\text{-D}} C f. \quad (16)$$

Here, $D_{1\text{-D}}$ is an $S \times S$ diagonal matrix defined as

$$D_{1\text{-D}} = \text{diag}\left[\underbrace{e^{j\phi_{1\text{-D}}(1)}, \ldots, e^{j\phi_{1\text{-D}}(1)}}_{K}, \underbrace{e^{j\phi_{1\text{-D}}(2)}, \ldots, e^{j\phi_{1\text{-D}}(2)}}_{K}, \right.$$
$$\left. \ldots, \underbrace{e^{j\phi_{1\text{-D}}(M)}, \ldots, e^{j\phi_{1\text{-D}}(M)}}_{K} \right]. \quad (17)$$

These relationships can also be stated as follows:

$$\bar{r}_{\epsilon_m} = e^{j\phi_{1\text{-D}}(m)} \bar{r}_m \quad \bar{C}_m(\phi_{1\text{-D}}) f = e^{j\phi_{1\text{-D}}} \bar{C}_m f$$
$$\text{for} \quad m = 1, 2, \ldots, M. \quad (18)$$

Here, $\bar{r}_m$ and $\bar{C}_m$ are the error-free phase history data and the assumed model matrix for the mth cross-range position. Note that, in a 1-D cross-range phase error case, there are M unknowns; in a 2-D separable phase error case, there are $M + K$ unknowns;

and in a 2-D nonseparable phase error case, there are $S = MK$ unknowns. Hence, correcting for 2-D nonseparable phase errors is a much more difficult problem than the others.

IV. PROPOSED METHOD

Sparsity-driven radar imaging has already found use in a number of contexts [24]–[36]. In SAR applications, there is widespread use of sparsity-based imaging due to the advantages such as super-resolution and the artifact suppression that it provides. Such techniques assume that the observation model is known exactly. However, it is common to encounter model errors. In the presence of phase errors and additive measurement noise induced by the SAR system, the observation model becomes

$$g = C(\phi) f + v \quad (19)$$

where v stands for measurement noise, which is assumed to be white Gaussian noise and g is the noisy phase-corrupted observation data. Here, ϕ refers to one of the three types of phase errors introduced in Section III.

Based on these observations, we propose a nonquadratic regularization-based method for joint imaging and phase error correction. While existing sparsity-driven SAR imaging methods assume that data contain no phase errors, our approach jointly estimates and compensates such errors in the data while performing sparsity-driven image formation. In particular, we pose the problem of joint imaging and phase error estimation as the problem of minimizing the following cost function:

$$J(f, \phi) = \|g - C(\phi) f\|_2^2 + \lambda \|f\|_1. \quad (20)$$

Here, λ is the regularization parameter, which specifies the strength of the contribution of the regularization term into the solution. The given cost function is minimized jointly with respect to f and ϕ using a coordinate descent technique. The algorithm is an iterative algorithm, which cycles through steps of image formation and phase error estimation and compensation. Every iteration involves two steps. In the first step, the cost function is minimized with respect to the field, and in the second step, the phase error is estimated given the field estimate. Before the algorithm passes to the next iteration, the model matrix is updated using the estimated phase error. This flow is outlined in Algorithm 1.

In Algorithm 1, n denotes the iteration number. $\hat{f}^{(n)}$ and $\hat{\phi}^{(n)}$ are the image and phase error estimates at iteration n, respectively. Note that the knowns in this algorithm are the noisy phase-corrupted data g and the initially assumed model matrix C. The unknowns are the field f and the phase error ϕ together with the associated model matrix $C(\phi)$ that takes the phase errors into account. It is worth noting here that the use of the nonquadratic regularization-based framework contributes to the accurate estimation of the phase errors as well. Although nonquadratic regularization by itself cannot completely handle the kinds of phase errors considered in this paper, it exhibits some

robustness to small perturbations on the observation model matrix [37]. In the context of our approach, the nonquadratic regularization term in the cost function provides a small amount of focusing of the estimated field in each iteration. This focusing then enables better estimation of the phase error. This in turn results in a more accurate observation model matrix, which provides better data fidelity and leads to a better field estimate in the next iteration.

Algorithm 1 Algorithm for the Proposed SDA Method

Initialize $n = 0 \hat{f}^{(0)} = C^H g$ and $C(\hat{\phi}^{(0)}) = C$

1. $\hat{f}^{(n+1)} = \arg\min_f J(f, \hat{\phi}^{(n)})$

2. $\hat{\phi}^{(n+1)} = \arg\min_\phi J(\hat{f}^{(n+1)}, \phi)$

3. Update $C(\hat{\phi}^{(n+1)})$ using $\hat{\phi}^{(n+1)}$ and C.

4. Let $n = n + 1$ and return to 1.

Stop when $\|\hat{f}^{(n+1)} - \hat{f}^{(n)}\|_2^2 / \|\hat{f}^{(n)}\|_2^2$ is less than a predetermined threshold.

In this paper, the value of the threshold is chosen as 10^{-3}.

Next, we provide the details of the algorithm for the three classes of phase errors described in Section III.

A. Algorithm for 1-D Phase Errors

In the algorithm for 1-D phase errors, in the first step of every iteration, the following cost function is minimized with respect to f:

$$\hat{f}^{(n+1)} = \arg\min_f \left\| g - C\left(\hat{\phi}_{1\text{-}D}^{(n)}\right) f \right\|_2^2 + \lambda \|f\|_1. \quad (21)$$

This is the image formation step and is the same for all types of phase errors. To avoid problems due to nondifferentiability of the l_1-norm at the origin, a smooth approximation is used [20] as follows:

$$\|f\|_1 \approx \sum_{i=1}^{I} \left(|f_i|^2 + \beta\right)^{1/2} \quad (22)$$

where β is a nonnegative small constant. In each iteration, the field estimate is obtained as

$$\hat{f}^{(n+1)} = \left(C\left(\hat{\phi}_{1\text{-}D}^{(n)}\right)^H C\left(\hat{\phi}_{1\text{-}D}^{(n)}\right) + \lambda W\left(\hat{f}^{(n)}\right)\right)^{-1} C\left(\hat{\phi}_{1\text{-}D}^{(n)}\right)^H g \quad (23)$$

where $W(\hat{f}^{(n)})$ is a diagonal matrix, i.e.,

$$W(\hat{f}^{(n)}) = \text{diag}\left[1/\left(\left|\hat{f}_i^{(n)}\right|^2 + \beta\right)^{1/2} \dots 1/\left(\left|\hat{f}_I^{(n)}\right|^2 + \beta\right)^{1/2}\right]. \quad (24)$$

The matrix inversion in (23) is not carried out explicitly but rather numerically, through the conjugate gradient algorithm. Note that this algorithm has been used in a variety of settings for sparsity-driven radar imaging and has been shown to be a descent algorithm [38].

The second step involves phase error estimation, in which a different procedure is implemented for each type of phase errors. For 1-D cross-range-varying phase errors, given the field estimate, the following cost function is minimized for every cross-range position [39]

$$\hat{\phi}_{1\text{-}D}^{(n+1)}(m) = \arg\min_{\phi_{1\text{-}D}(m)} \left\| \bar{g}_m - e^{(j\phi_{1\text{-}D}(m))} \bar{C}_m \hat{f}^{(n+1)} \right\|_2^2 \quad \forall m \quad (25)$$

where $\hat{\phi}_{1\text{-}D}^{(n+1)}(m)$ denotes the phase error estimate for the cross-range position m in the iteration $(n + 1)$. In (25), the $K \times 1$ vector $\bar{g}_m$ is the noisy SAR data at the mth cross-range position. After evaluating the norm expression in (25) (see Appendix for details), we obtain the following:

$$\hat{\phi}_{1\text{-}D}^{(n+1)}(m)$$
$$= \arg\min_{\phi_{1\text{-}D}(m)} \left(\bar{g}_m^H \bar{g}_m - 2\sqrt{\Re^2 + \Im^2} \cos \right.$$
$$\times \left[\phi_{1\text{-}D}(m) + \arctan\left(\frac{-\Im}{\Re}\right) \right]$$
$$\left. + \hat{f}^{(n+1)H} \bar{C}_m^H \bar{C}_m \hat{f}^{(n+1)} \right) \quad (26)$$

where

$$\Re = Re\left\{ \hat{f}^{(n+1)H} \bar{C}_m^H \bar{g}_m \right\} \quad \Im = Im\left\{ \hat{f}^{(n+1)H} \bar{C}_m^H \bar{g}_m \right\}. \quad (27)$$

We know that negative cosine has its minimum at zero and integer multiples of 2π; therefore, if we set the argument of the cosine to zero, we can find the phase error estimate in a closed form, as given in (28), for the corresponding aperture position:

$$\hat{\phi}_{1\text{-}D}^{(n+1)}(m) = -\arctan\left(\frac{-\Im}{\Re}\right). \quad (28)$$

Using the phase error estimate, the model matrix is updated as follows:

$$\bar{C}_m\left(\hat{\phi}_{1\text{-}D}^{(n+1)}(m)\right) = e^{\left(j\hat{\phi}_{1\text{-}D}^{(n+1)}(m)\right)} \bar{C}_m \quad \forall m. \quad (29)$$

We increment n and turn back to the optimization problem in (21).

Moreover, note that phase updates are performed after each step of the f-iteration in (23); as a result of which, the overall computational load of our approach is not significantly more than that of just image formation.

B. Algorithm for 2-D Separable Phase Errors

In case of 2-D separable phase errors, the field estimate is obtained via minimizing the following cost function:

$$\hat{f}^{(n+1)} = \arg\min_f \left\| g - C\left(\hat{\phi}_{2\text{-}D-s}^{(n)}\right) f \right\|_2^2 + \lambda \|f\|_1. \quad (30)$$

Given the field estimate, first, the phase error in the cross-range direction γ is estimated using the 1-D phase error estimation procedure described in Section IV-A; then, this estimate is used to update the model matrix as follows:

$$\hat{\gamma}(m)^{(n+1)} = \arg\min_{\gamma(m)} \left\| \bar{g}_m - e^{(j\gamma(m))} \bar{C}_m \hat{f}^{(n+1)} \right\|_2^2 \quad \forall m \quad (31)$$

$$\bar{C}_m\left(\hat{\gamma}(m)^{(n+1)}\right) = e^{(j\hat{\gamma}(m)^{(n+1)})} \bar{C}_m \quad \forall m. \quad (32)$$
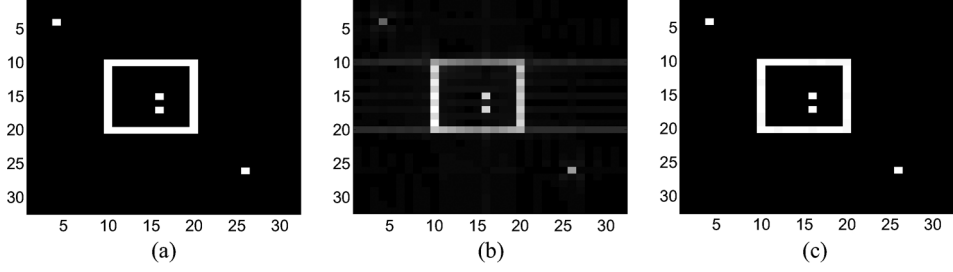
Fig. 2.   (a) The original scene. (b) Conventional imaging from the data without phase errors. (c) Sparsity-driven imaging from the data without phase errors.
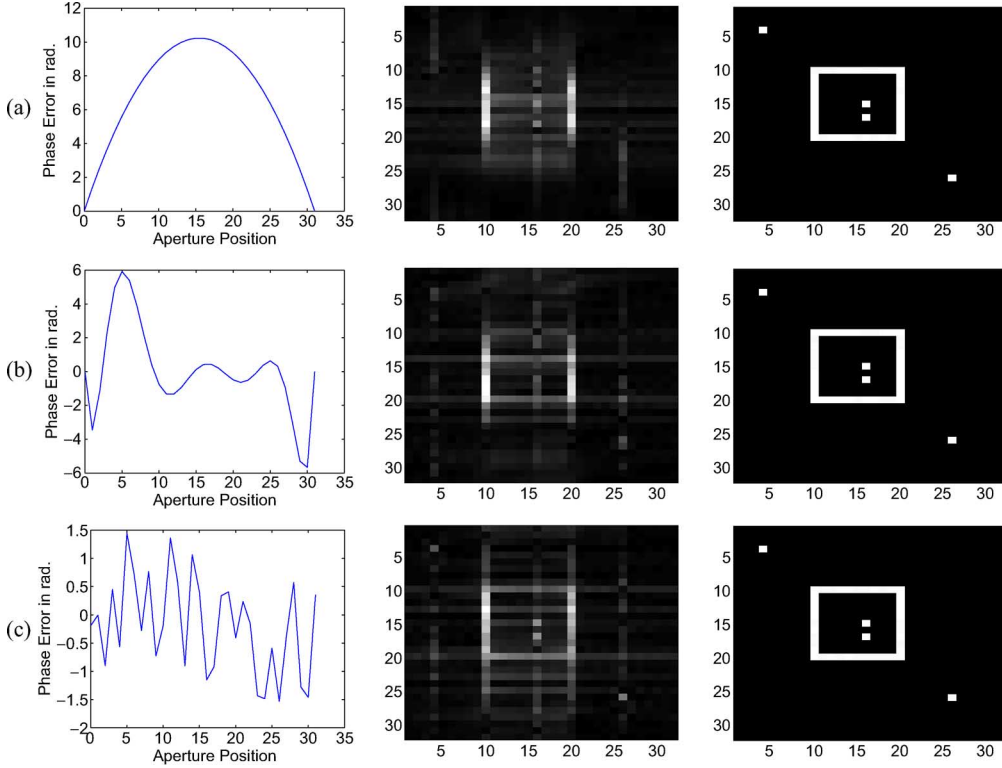

Fig. 3.   Left- Phase error. Middle- Images reconstructed by conventional imaging. Right- Images reconstructed by the proposed SDA method. (a) Results for quadratic phase error. (b) Results for an 8th order polynomial phase error. (c) Results for a phase error uniformly distributed in $[-\pi/2, \pi/2]$.

Then, to estimate the phase error in the range direction, the elements of the data vector g and the rows of the model matrix $C(\hat{\gamma}^{(n+1)})$ are ordered in such a way that the elements and rows corresponding to the same range position lie under each other. Let these modified data vector and modified model matrix be g_{mod} and C_{mod}, respectively (i.e., the phase history matrix is row stacked rather than column stacked). Using these new variables, the phase error estimate $\hat{\xi}$ for the range direction is found repeating the same procedure as in the cross-range direction and, this time, for every range position. This can be expressed as follows:

$$\hat{\xi}(k)^{(n+1)}$$
$$= \arg \min_{\xi(k)} \left\| \bar{g}_{\mathrm{mod}_k} - e^{(j\xi(k))} \bar{C}_{\mathrm{mod}_k} \hat{f}^{(n+1)} \right\|_2^2 \quad \forall k \quad (33)$$

$$\bar{C}_{\mathrm{mod}_k} \left(\hat{\xi}(k)^{(n+1)} \right)$$
$$= e^{(j\hat{\xi}(k)^{(n+1)})} \bar{C}_{\mathrm{mod}_k} \quad \forall k. \quad (34)$$

Here, $\bar{g}_{\mathrm{mod}_k}$ and $\bar{C}_{\mathrm{mod}_k}$ represent the parts of g_{mod} and C_{mod} corresponding to a particular range position k, respectively. To return to the original form, the rows of the matrix $C_{\mathrm{mod}}(\hat{\xi}^{(n+1)})$

are rearranged so that the rows corresponding to the same cross-range position lie under each other. This rearranged matrix is denoted by $C(\hat{\phi}_{2\text{-D}-s}^{(n+1)})$, which is used in the next iteration to find the next field estimate.

C. Algorithm for 2-D Nonseparable Phase Errors

In a more general case in which we consider 2-D nonseparable phase errors, the image formation step of the algorithm is essentially identical to its counterpart in previous cases. To obtain the field estimate, the following cost function is minimized with respect to f:

$$\hat{f}^{(n+1)} = \arg \min_f \left\| g - C\left(\hat{\phi}_{2\text{-D}-ns}^{(n)} \right) f \right\|_2^2 + \lambda \|f\|_1. \quad (35)$$

Using the same point of view as in the previous two cases, in the phase error estimation step, the following cost function is minimized [40]:

$$\hat{\phi}_{2\text{-D}-ns}^{(n+1)}(s)$$
$$= \arg \min_{\phi_{2\text{-D}-ns}(s)} \left\| g(s) - e^{(j\phi_{2\text{-D}-ns}(s))} C_s \hat{f}^{(n+1)} \right\|_2^2 \quad \forall s. \quad (36)$$
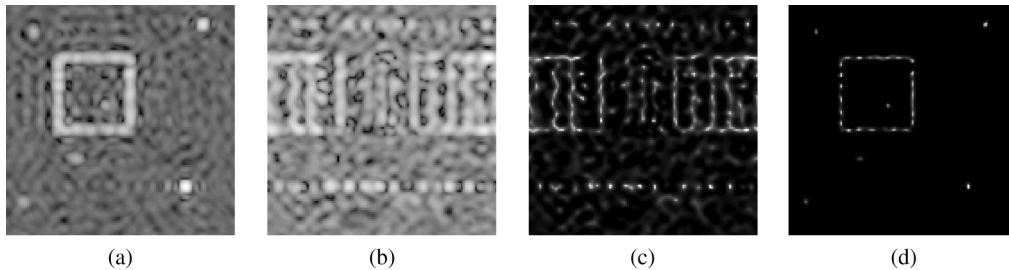
Fig. 4. Experimental results on a speckled scene. (a) Conventional image reconstructed from noisy data without phase error. (b) Conventional image reconstructed from noisy data with phase error. (c) Image reconstructed by sparsity-driven imaging from noisy data with phase error. (d) Image reconstructed by the proposed SDA method.

carrier frequency (ω_0)	$2\pi \times 10^{10}\ rad/s$
chirp rate (2α)	$2\pi \times 10^{12}\ rad/s^2$
pulse duration (T_p)	$4 \times 10^{-4} sec.$
angular range $(\Delta\theta)$	2.3^o

Here, $\hat{\phi}_{\text{2-D}-ns}^{(n+1)}(s)$ denotes the phase error estimate for the sth data sample in iteration $(n+1)$. This step is solved in the closed form in a similar way to that in (25). In particular, the solution of the optimization problem in (36) is as follows:

$$\hat{\phi}_{\text{2-D}-ns}^{(n+1)}(s) = -\arctan\left(\frac{-\Im}{\Re}\right) \qquad (37)$$

where

$$\Re = Re\left\{\hat{f}^{(n+1)^H} C_s^H g(s)\right\} \quad \Im = Im\left\{\hat{f}^{(n+1)^H} C_s^H g(s)\right\}. \qquad (38)$$

Using the phase error estimate, the model matrix is updated through:

$$C_s\left(\hat{\phi}_{\text{2-D}-ns}^{(n+1)}(s)\right) = e^{\left(j\hat{\phi}_{\text{2-D}-ns}^{(n+1)}(s)\right)} C_s \quad \forall s. \qquad (39)$$

If the phase error type (i.e., 1-D, 2-D separable, or 2-D nonseparable) is known, then it is natural to use the corresponding version of the proposed algorithm for best phase error estimation performance. If the phase error type is not known *a priori*, then the version of our algorithm for the 2-D nonseparable case can be used since this is the most general scenario. For any of these three types of phase errors, our algorithm does not require any knowledge about how the phase error function varies (randomly, quadratically, polynomially, etc.) along the range (in 2-D cases) or cross-range (in 1-D and 2-D cases) directions. We demonstrate the effectiveness of our approach on data corrupted by various phase error functions.

V. Experimental Results

We have applied the proposed SDA method in a number of scenarios and present our results in the following two subsections. In Section V-A, we present our results on various types of data and demonstrate the improvements in visual image quality, as compared with the uncompensated case. In Section V-B, we
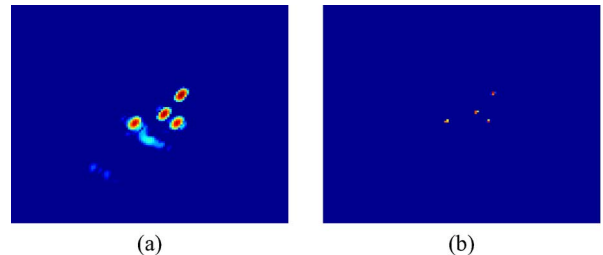

Fig. 5. (a) Conventional imaging from the data without phase error. (b) Sparsity-driven imaging from the data without phase error.

provide a quantitative comparison of our approach with existing state-of-the-art autofocus techniques.

A. Qualitative Results and Comparison to the Uncompensated Case

To present qualitative results for the proposed method in comparison to the uncompansated case, several experiments have been performed on various synthetic scenes as well as on two public SAR data sets provided by the U.S. Air Force Research Laboratory (AFRL): the Slicy data, which is part of the MSTAR data set [41], and the Backhoe data [42].

To generate synthetic SAR data for a 32×32 scene, we have used a SAR system model with the parameters given in Table I. The resulting phase history data lie on a polar grid. As observation noise, complex white Gaussian noise is added to the data so that SNR is 30 dB. We have performed experiments for four different types of phase errors. The original synthetic image is shown in Fig. 2(a). For the data without phase errors, conventional and sparsity-driven reconstructions are given in Fig. 2(b) and (c), respectively. In this paper, in all of the experiments, the polar-format algorithm is used for conventional imaging. Results by conventional imaging and by the proposed method for different types of phase errors are shown in Fig. 3. Conventionally reconstructed images suffer from degradation due to phase errors. The results show the effectiveness of the proposed method. As shown in Fig. 3, it is not possible to visually distinguish the images formed by the proposed method from the original scene.

To demonstrate the performance of SDA in the presence of speckle, we present some results on a 128×128 synthetic scene in Fig. 4. The scene consists of six pointlike targets and a spatially extended target with the shape of a square frame. To create speckle, a random phase is added to the reflectivities of
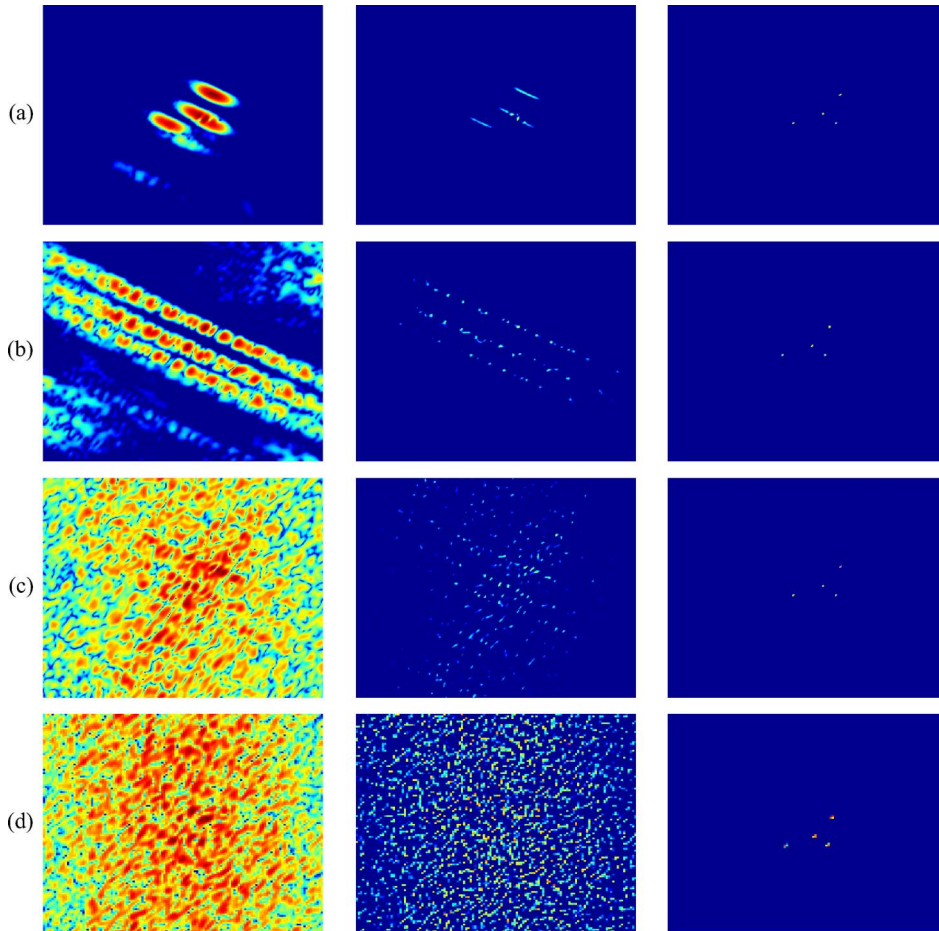
Fig. 6. Left- Images reconstructed by conventional imaging. Middle- Images reconstructed by sparsity-driven imaging. Right- Images reconstructed by the proposed SDA method. (a) Results for a 1-D quadratic phase error. (b) Results for a 1-D phase error uniformly distributed in $[-\pi, \pi]$. (c) Results for a 2-D separable phase error composed of two 1-D phase errors uniformly distributed in $[-3\pi/4, 3\pi/4]$. (d) Results for a 2-D non-separable phase error uniformly distributed in $[-\pi, \pi]$.

the underlying scene. The corresponding SAR data are simulated by taking a 32×32 band-limited segment from the 2-D Fourier transform of the scene. Then a 1-D cross-range-varying random phase error, i.e., uniformly distributed in $[-\pi, \pi]$, has been added to the data. The speckle is clearly visible in the conventional image reconstructed from the data without phase errors in Fig. 4(a). The images reconstructed by conventional imaging and sparsity-driven imaging when the data are corrupted by phase errors are shown in Fig. 4(b) and (c), respectively. The result in Fig. 4(d) demonstrates that SDA can effectively perform imaging and phase error compensation in the presence of speckle.

In Fig. 5, we present the images reconstructed from the Slicy data without phase errors. The Slicy target is a precisely designed and machined engineering test target containing multiple simple geometric radar reflector static shapes. Fig. 5(a) shows the image reconstructed conventionally, and Fig. 5(b) shows the result of sparsity-driven imaging. As seen in the figures, sparsity-driven imaging provides high-resolution images with enhanced features (in this particular example, this means locations of dominant point scatterers). Fig. 6(a) and (b) shows the results on the Slicy data for a 1-D quadratic and a 1-D random phase error, which is uniformly distributed in $[-\pi, \pi]$. The images in the middle column correspond to the direct applica-
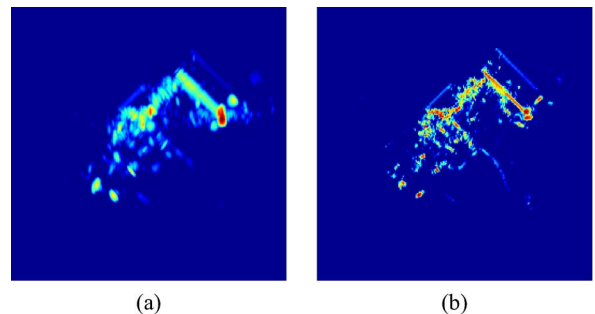

Fig. 7. (a) Conventional imaging from the data without phase error. (b) Sparsity-driven imaging from the data without phase error.

tion of the sparsity-driven imaging technique of [20] without model error compensation. The significant degradation in the reconstructions show that sparsity-driven imaging without model error compensation cannot handle phase errors. From the images presented in the right column, we can see clearly that the images formed by the proposed SDA method inherit and exhibit the advantages of sparsity-driven imaging [see Fig. 5(b)], and in the meantime, the phase errors are removed as well. In Fig. 6(c) and (d), the results for 2-D separable and nonseparable random phase errors are displayed. 2-D phase errors cause a dramatic degradation on the reconstructed images. However, the
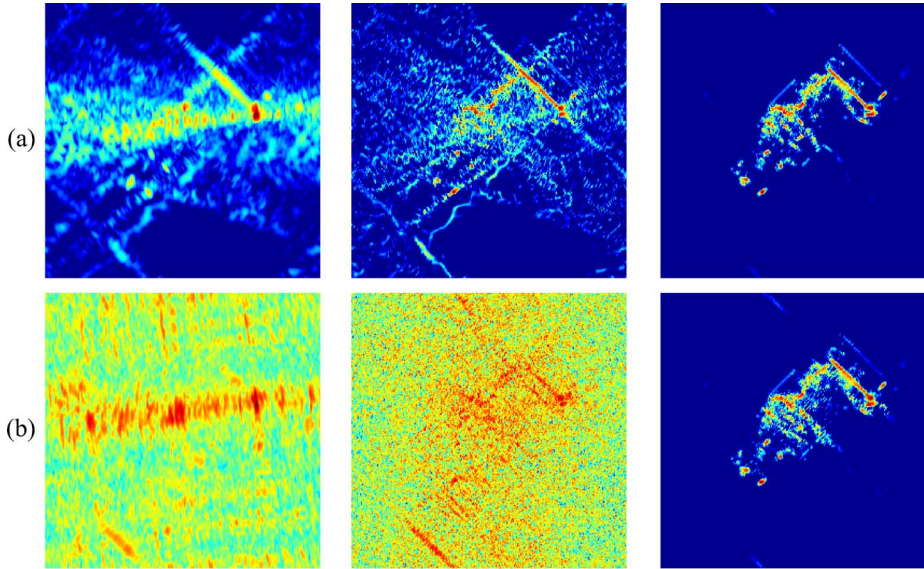
Fig. 8. Left- Images reconstructed by conventional imaging. Middle- Images reconstructed by sparsity-driven imaging. Right- Images reconstructed by the proposed SDA method. (a) Results for a 1-D phase error uniformly distributed in $[-\pi/2, \pi/2]$. (b) Results for a 2-D separable phase error composed of two 1-D phase errors uniformly distributed in $[-3\pi/4, 3\pi/4]$.
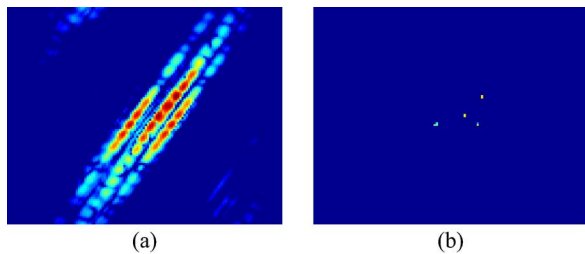

Fig. 9. Experiments on the Slicy data with 70% frequency band omissions : (a) Conventional imaging from the data without phase error. (b) Sparsity-driven imaging from the data without phase error.

proposed SDA method successfully corrects the 2-D phase errors as well and produces images that exhibit accurate localization of the true scatterers and significant artifact suppression.

Another data set on which we present results is the Backhoe data set. We present 2-D image reconstruction experiments based on the AFRL "Backhoe Data Dome, Version 1.0," which consists of a simulated wideband (7–13 GHz), full polarization, complex backscatter data from a backhoe vehicle in free space. The backscatter data are available over a full upper 2π steradian viewing hemisphere. In our experiments, we use VV polarization data, i.e., centered at 10 GHz, and with an azimuthal span of 110°. The data we use in our experiments have a bandwidth of 1 GHz. To deal with the wide-angle observation in the Backhoe data set, we incorporate the subaperture-based composite imaging approach of [43] into our framework. The composite image is formed by combining the subaperture images so that each pixel value of the composite image is determined by selecting the maximum value for that pixel across the subaperture images. For this experiment, phase error estimation and correction are performed for every subaperture image. In Fig. 7, we show the conventionally and sparsity-driven reconstructed images for the data without a phase error. The results on Backhoe data for 1-D and 2-D separable random

phase errors are presented in Fig. 8. In the left and middle columns of Fig. 8, the artifacts due to phase errors are clearly seen in the images reconstructed by conventional imaging and sparsity-driven imaging, respectively. However, both 1-D and 2-D phase errors are compensated effectively by the proposed method. From the given examples so far, we see that the proposed SDA method corrects the phase errors effectively and provides images with high resolution and reduced sidelobes, due to the nonquadratic regularization-based framework.

We mentioned that regularization-based imaging gives satisfying results in cases of incomplete data as well. We explore this aspect in the presence of phase errors performing an experiment on Slicy data with frequency-band omissions. In this experiment, data from randomly selected contiguous frequency bands corresponding to 70% of frequencies have been set to zero, i.e., only 30% of the spectral data within the radar's bandwidth are available. A detailed explanation of this spectral masking procedure can be found in [43]. Then, a 1-D quadratic phase error function was applied to the data. The results of this experiment are presented in Figs. 9 and 10. As shown from the reconstructions, the proposed method produces feature enhanced images and removes phase errors effectively even when the data are partially available.

Finally, we demonstrate how the nonquadratic regularization functional in our framework supports phase error compensation, through a simple experiment in which we compare the results of our approach with a quadratic regularization scheme. In this experiment, we have applied a 1-D cross-range-varying random phase error, which is uniformly distributed in $[-\pi, \pi]$ to the data from a synthetic scene simulated just by taking its 2-D Fourier transform. To construct a quadratic regularization-based scheme, we have replaced the l_1-norm in our approach with an l_2-norm without changing the phase error estimation piece. We present the results of this experiment in Fig. 11. As shown in the images, with the quadratic regularization approach, it is not possible to correct phase errors, whereas the image reconstructed
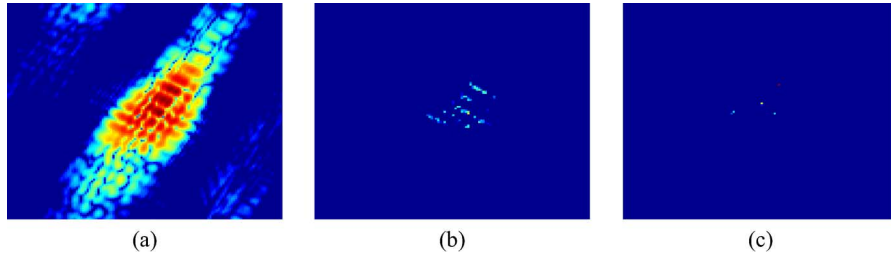
Fig. 10. Experiments on the Slicy data with 70% frequency band omissions and 1-D quadratic phase error: (a) Conventional imaging. (b) Sparsity-driven imaging (c) Proposed SDA method.
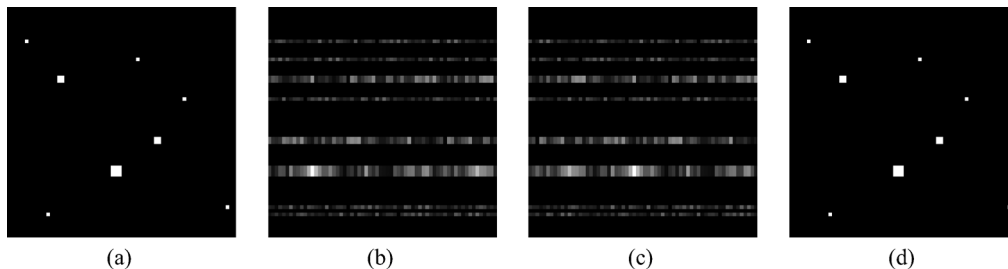

Fig. 11. Results of the experiment for testing the effect of the nonquadratic regularization term in the proposed SDA method on phase error compensation. (a) The original scene. (b) Conventional imaging from the data with phase error. (c) Image reconstructed in the case of replacing the l_1-norm in our approach with an l_2-norm without changing the phase error estimation piece. (d) Image reconstructed by the proposed SDA method.

by our nonquadratic regularization-based SDA algorithm is perfectly focused.

B. Quantitative Results in Comparison to State-of-the-Art Autofocus Methods

In the second part of the experimental study, we present results for comparison of the proposed technique with existing autofocus techniques. In Fig. 12, we show comparative results for a 64×64 synthetic scene. The SAR data are simulated by taking a band-limited segment on a rectangular grid from the 2-D discrete Fourier transform of the scene. Then, complex white Gaussian noise is added to the data so that the input SNR is 10.85 dB. Then, a 1-D cross-range-varying random phase error, which is uniformly distributed in $[-\pi, \pi]$, is added to the data. The performance of the proposed technique is compared with the performance of PGA [2] and entropy minimization techniques [3], [5]–[7]. For entropy minimization, we have used the procedure given in [5]. For this particular experiment, the results suggest that all three methods do a good job in estimating the phase error. However, in terms of image quality, while PGA and entropy minimization are limited by conventional imaging, the proposed SDA method demonstrates the advantage of joint sparsity-driven imaging and phase error correction and produces a scene that appears to provide a very accurate representation of the original scene. For the same synthetic scene, we have also performed experiments with different input SNRs. For each SNR value, we have applied 20 different random 1-D phase errors, where all of them uniformly distributed in $[-\pi, \pi]$. For each experiment, we compute three different metrics. These are the MSE between the original image and the image resulting from the application of the autofocus technique considered, target-to-background ratio, and metrics for the phase error estimation error. These metrics are computed as follows:

$$\text{MSE} = \frac{1}{I} \left\| |f| - |\hat{f}| \right\|_2^2. \tag{40}$$

Here, f and $\hat{f}$ denote the original and the reconstructed images, respectively. I is the total number of pixels.

The target-to-background ratio is used to determine the accentuation of the target pixels with respect to the background:

$$\text{TBR} = 20 \log_{10} \left(\frac{\max_{i \in T} |\hat{f}_i|}{\frac{1}{I_B} \sum_{j \in B} |\hat{f}_j|} \right). \tag{41}$$

Here, T and B denote the pixel indices for the target and the background regions, respectively. I_B is the number of background pixels.

To compare the phase error estimation performance of the proposed method to other techniques, we first compute the estimation error for phase errors as follows:

$$\phi_e = \phi - \hat{\phi}. \tag{42}$$

Here, ϕ_e is effectively the phase error that remains in the problem after correction of the data or the model using the estimated phase error. To evaluate various techniques based on their phase error estimation performance, it makes sense to first remove the components in ϕ_e that either have no effect on the reconstructed image or that can be easily dealt with, and then perform the evaluation based on the remaining error. We first note that a constant (as a function of the aperture position) phase shift has no effect on the reconstructed image [1]. Second, a linear phase shift does not cause blurring but rather a spatial shift in the reconstructed image. Such a phase error can be compensated by appropriate spatial operations on the scene [4], which we perform prior to quantitative evaluation. To disregard the effect of any constant phase shift in our evaluation, and also noting that the amount of variation of the phase error across the
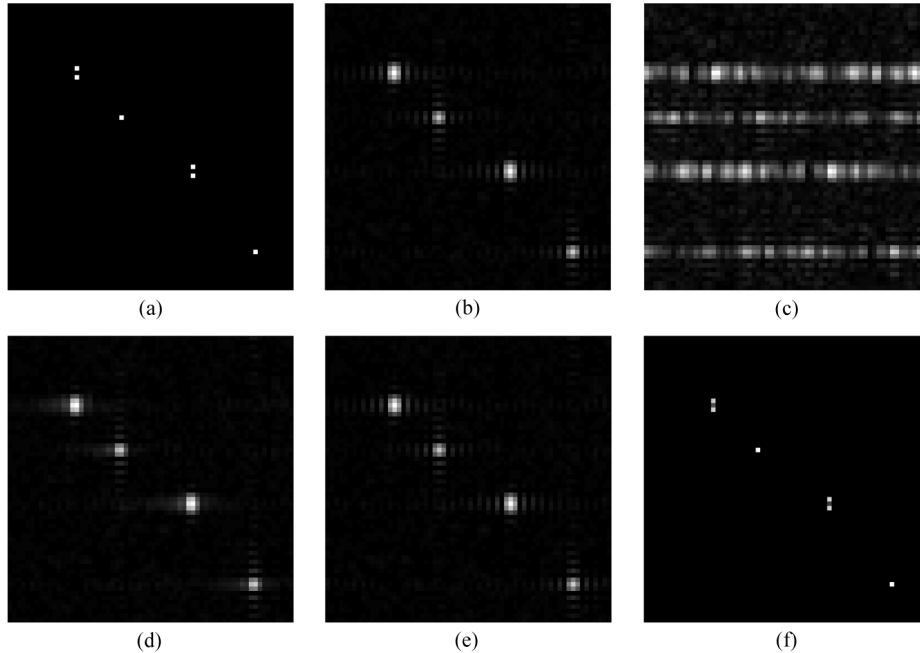
Fig. 12. (a) The original scene. (b) Conventional imaging from noisy data without phase error. (c) Conventional imaging from noisy data with phase error. (d) Result of PGA. (e) Result of entropy minimization. (f) Result of the proposed SDA method.
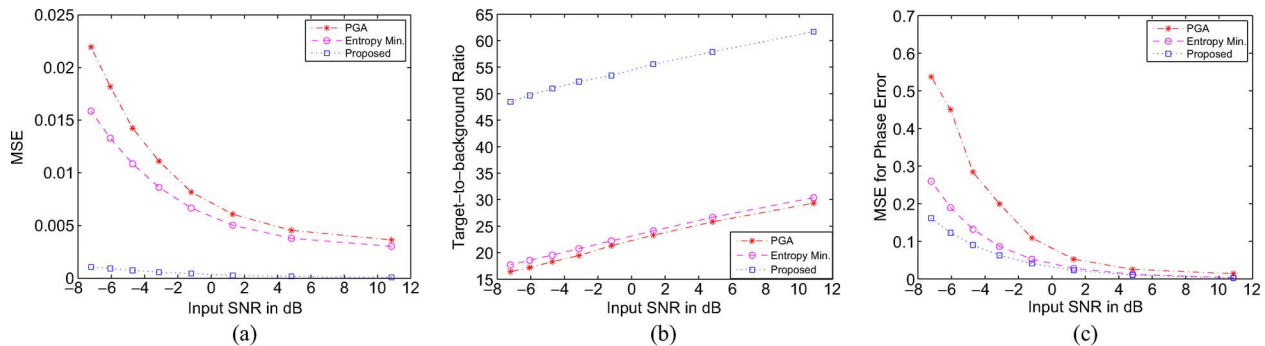

Fig. 13. Quantitative evaluation of the reconstruction of the scene in Fig. 12(a) for various SNRs. Each point on the curves corresponds to an average over 20 experiments with different random 1-D phase errors uniformly distributed in $[-\pi, \pi]$. (a) MSE versus SNR. (b) Target-to-background ratio versus SNR. (c) MSE for phase error estimations versus SNR.

aperture is closely related to the degree of degradation of the formed imagery, we propose using evaluation metrics based on the total variation (TV) of ϕ_e and on the l_2-norm of the gradient of ϕ_e:

$$\text{TV}_{PE} = \frac{1}{M-1}\|\nabla\phi_e\|_1 \quad \text{MSE}_{PE} = \frac{1}{M-1}\|\nabla\phi_e\|_2^2. \quad (43)$$

Here, $\nabla\phi_e$ is the $(M-1) \times 1$ vector, obtained by taking first-order differences between successive elements of ϕ_e. M is the total number of cross-range positions.

Now, we get back to the quantitative evaluation of the reconstruction of the scene in Fig. 12(a) for various SNRs. We present the comparison results for these three metrics in Fig. 13. Since TV_{PE} and MSE_{PE} values are similar for these particular experiments, for the sake of space, we show the results for MSE_{PE} only. From the plots presented, it is clearly seen that the proposed method performs better than the other techniques, particularly for low SNR values. We also note in Fig. 13(a) that the proposed SDA method yields much better performance in terms of the MSE between the original and the reconstructed

images even at high SNRs. This is due to the fact that SDA benefits from the advantages of sparsity-driven imaging (unlike the other techniques) over conventional imaging (see Fig. 12) in addition to successfully correcting the phase errors (similar to the other techniques) at high SNRs.

All of the three algorithms were implemented using nonoptimized Matlab code on an Intel Celeron 2.13-GHz CPU. In the experiment of Fig. 12, the computation times required by PGA, entropy minimization, and the proposed SDA method are 0.624, 1.1076, and 2.1216 s, respectively. For the experiments of Fig. 13, the average computation times for PGA, entropy minimization, and SDA are 0.3095, 0.4719, and 3.4961 s, respectively. The computational load of SDA is relatively more than the other methods, but this can be justified through the benefits provided by the sparsity-driven imaging framework underlying SDA, as demonstrated in our experiments.

In Fig. 14, we display some comparative results on the Backhoe data as well. For this experiment, the applied 1-D phase error is a random error with a uniform distribution in $[-\pi, \pi]$. In this example, for quantitative comparison, we use
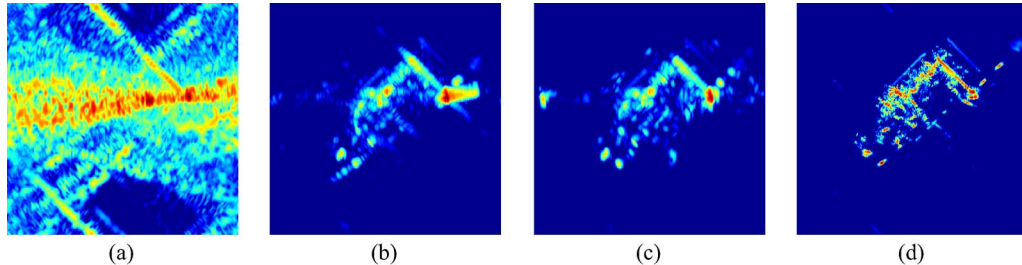
Fig. 14. Experiments on the Backhoe data for a 1-D random phase error with a uniform distribution in $[-\pi, \pi]$. (a) Conventional imaging with phase error. (b) Result of PGA. (c) Result of entropy minimization. (d) Result of the proposed SDA method.
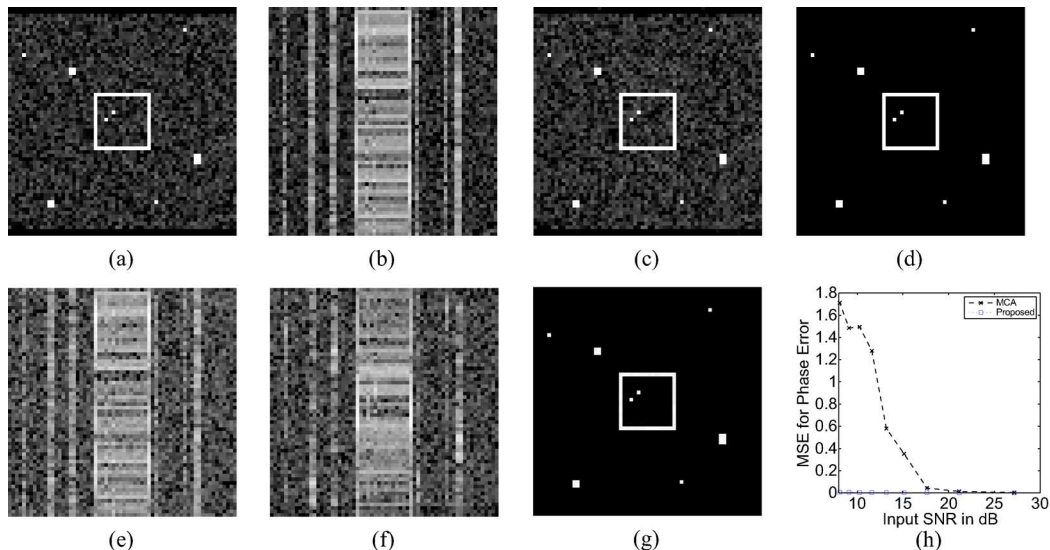

Fig. 15. (a) The original scene. (b) Conventional imaging from noisy phase-corrupted data for input SNR of 27 dB. (c) Result of MCA for input SNR of 27 dB. (d) Result of the proposed SDA method for input SNR of 27 dB. (e) Conventional imaging from noisy phase-corrupted data for input SNR of 10 dB. (f) Result of MCA for input SNR of 10 dB. (g) Result of the proposed SDA method for input SNR of 10 dB. (h) MSEs for phase error estimation versus SNR.

TABLE II
MSE ACHIEVED BY VARIOUS METHODS IN ESTIMATING THE PHASE ERROR
FOR THE BACKHOE EXPERIMENT IN FIG. 14

	PGA	Entropy Minimization	Proposed SDA Method
MSE_{PE}	3.3267	2.1715	2.1382

the MSE for the phase error. The MSE_{PE} values are shown in Table II.

The results show that the proposed method performs phase error estimation more accurately than PGA and entropy minimization techniques. Furthermore, the proposed method also exhibits superiority over existing autofocus techniques in terms of the quality of the reconstructed scene. In particular, the proposed method results in a finer and more detailed visualization through noise and sidelobe suppression as well as resolution improvements. The reconstructed images and quantitative comparison show the effectiveness of the proposed approach.

Finally, we compare our method with the recently proposed MCA technique [12]. We have generated a 64×64 synthetic scene that satisfies the requirements of MCA, involving a condition on the rank of the image, as well as the presence of a low-return region in the scene. The SAR data used in these experiments are corrupted by a 1-D cross-range-varying random phase error, which is uniformly distributed in $[-\pi, \pi]$. We show the results of the experiments performed for various input SNR

levels in Fig. 15. We observe that both MCA and SDA perform successful phase error compensation at the relatively high SNR of 27 dB (see Fig. 15(c) and (d)). However, when SNR is reduced to 10 dB, MCA is not able to correct the phase error, as shown in Fig. 15(f). On the other hand, SDA compensates phase errors, and suppresses noise and clutter effectively even for this relatively low SNR case, as shown in Fig. 15(g). Fig. 15(h) contains a plot of MSEs for phase error estimation achieved by MCA and SDA on this scene for various SNR levels. This plot demonstrates the robustness of SDA to noise. Average computation times required by MCA and the proposed SDA method for the experiments displayed in Fig. 15 are 0.1629 and 2.5151 s, respectively (using nonoptimized Matlab code on an Intel Celeron 2.13-GHz CPU). The results of these experiments show that, although MCA is a fast algorithm and works very well in scenarios involving high-quality data, its performance degrades significantly as the SNR decreases.

VI. CONCLUSION

We have proposed and demonstrated a sparsity-driven technique for joint SAR imaging and phase error correction. The method corrects the phase errors during the image formation process while it produces high-resolution focused SAR images, due to its sparsity enforcing nature resulting from the use of a

nonquadratic regularization-based framework. While the proposed SDA method requires more computation compared with existing autofocus techniques due to its sparsity-driven image formation part, its overall computational load is not significantly more than that of sparsity-driven imaging without phase error compensation since image formation and phase error estimation are performed simultaneously in the proposed method. The method can handle 1-D as well as 2-D phase errors. Experimental results on various scenarios demonstrate the effectiveness of the proposed approach as well as the improvements that it provides over existing methods for phase error correction.

In this paper, we have considered SAR, but our approach is applicable in other areas, where similar types of model errors are encountered as well. Since the proposed method has a sparsity-driven structure, it is applicable only to radar imaging scenarios in which the underlying scene admits a sparse representation in a particular domain. Other potential extensions may be the formulation of the problem for scenarios involving sparse representations of the field in various spatial dictionaries or incorporation of prior information or some constraints on phase error. For future work, model errors in multistatic scenarios and target-motion-induced phase errors would be of interest as well.

<div align="center">APPENDIX</div>

In this Appendix, we describe how we get from (25) to (26). The cost function in (25) for phase error estimation is as follows:

$$\hat{\phi}_{1\text{-}D}^{(n+1)}(m) = \arg\min_{\phi_{1\text{-}D}(m)} \left\| \bar{g}_m - e^{(j\phi_{1\text{-}D}(m))} \bar{C}_m \hat{f}^{(n+1)} \right\|_2^2 \; \forall m.$$

Here, M denotes the total number of cross-range positions. When we evaluate the norm expression, we get

$$\left\| \bar{g}_m - e^{(j\phi_{1\text{-}D}(m))} \bar{C}_m \hat{f}^{(n+1)} \right\|_2^2$$
$$= \left(\bar{g}_m - e^{(j\phi_{1\text{-}D}(m))} \bar{C}_m \hat{f}^{(n+1)} \right)^H$$
$$\times \left(\bar{g}_m - e^{(j\phi_{1\text{-}D}(m))} \bar{C}_m \hat{f}^{(n+1)} \right)$$
$$= \bar{g}_m^H \bar{g}_m - \bar{g}_m^H e^{(j\phi_{1\text{-}D}(m))} \bar{C}_m \hat{f}^{(n+1)}$$
$$\quad - \hat{f}^{(n+1)H} \bar{C}_m^H \left(e^{(j\phi_{1\text{-}D}(m))} \right)^H \bar{g}_m$$
$$\quad + \hat{f}^{(n+1)H} \bar{C}_m^H \underbrace{\left(e^{(j\phi_{1\text{-}D}(m))} \right)^H e^{(j\phi_{1\text{-}D}(m))}}_{e^{(-j\phi_{1\text{-}D}(m))}} \bar{C}_m \hat{f}^{(n+1)}$$
$$= \bar{g}_m^H \bar{g}_m - \bar{g}_m^H \left[\cos(\phi_{1\text{-}D}(m)) + j\sin(\phi_{1\text{-}D}(m)) \right] \bar{C}_m \hat{f}^{(n+1)}$$
$$\quad - \hat{f}^{(n+1)H} \bar{C}_m^H \left[\cos(\phi_{1\text{-}D}(m)) - j\sin(\phi_{1\text{-}D}(m)) \right] \bar{g}_m$$
$$\quad + \hat{f}^{(n+1)H} \bar{C}_m^H \bar{C}_m \hat{f}^{(n+1)}$$
$$= \bar{g}_m^H \bar{g}_m - 2Re\left\{ \cos(\phi_{1\text{-}D}(m)) \hat{f}^{(n+1)H} \bar{C}_m^H \bar{g}_m \right\}$$
$$\quad + 2Re\left\{ j\sin(\phi_{1\text{-}D}(m)) \hat{f}^{(n+1)H} \bar{C}_m^H \bar{g}_m \right\}$$
$$\quad + \hat{f}^{(n+1)H} \bar{C}_m^H \bar{C}_m \hat{f}^{(n+1)}$$
$$= \bar{g}_m^H \bar{g}_m - 2\cos(\phi_{1\text{-}D}(m)) Re\left\{ \hat{f}^{(n+1)H} \bar{C}_m^H \bar{g}_m \right\}$$
$$\quad - 2\sin(\phi_{1\text{-}D}(m)) Im\left\{ \hat{f}^{(n+1)H} \bar{C}_m^H \bar{g}_m \right\}$$
$$\quad + \hat{f}^{(n+1)H} \bar{C}_m^H \bar{C}_m \hat{f}^{(n+1)}.$$

Let $Re\{\hat{f}^{(n+1)H} \bar{C}_m^H \bar{g}_m\} = \Re$ and $Im\{\hat{f}^{(n+1)H} \bar{C}_m^H \bar{g}_m\} = \Im$.

Since we can write $\sin(\phi_{1\text{-}D}(m))$ as $\cos(\phi_{1\text{-}D}(m) - (\pi/2))$, the equation becomes

$$\left\| \bar{g}_m - e^{j\phi_{1\text{-}D}(m)} \bar{C}_m \hat{f}^{(n+1)} \right\|_2^2$$
$$= \bar{g}_m^H \bar{g}_m - 2\left[\Re\cos(\phi_{1\text{-}D}(m)) + \Im\cos\left(\phi_{1\text{-}D}(m) - \frac{\pi}{2}\right) \right]$$
$$\quad + \hat{f}^{(n+1)H} \bar{C}_m^H \bar{C}_m \hat{f}^{(n+1)}.$$

The cosines in the previous equation can be added with the phasor addition rule to a single cosine. The phasors for terms $\Re\cos(\phi_{1\text{-}D}(m))$ and $\Im\cos(\phi_{1\text{-}D}(m) - (\pi/2))$ are as follows:

$$P_1 = Re^{j0} = \Re \quad P_2 = \Im e^{-\frac{j\pi}{2}} = -j\Im.$$

If we add phasors

$$P_1 + P_2 = \Re + (-j\Im) = \Re - j\Im$$

we can find the magnitude and the phase of the new cosine as

$$\text{magnitude} = \sqrt{\Re^2 + \Im^2} \qquad \text{phase} = \arctan\left(\frac{-\Im}{\Re}\right).$$

Finally, we can write

$$\left\| \bar{g}_m - e^{j\phi_{1\text{-}D}(m)} \bar{C}_m \hat{f}^{(n+1)} \right\|_2^2$$
$$= \bar{g}_m^H \bar{g}_m - 2\sqrt{\Re^2 + \Im^2} \cos\left[\phi_{1\text{-}D}(m) + \arctan\left(\frac{-\Im}{\Re}\right) \right]$$
$$\quad + \hat{f}^{(n+1)H} \bar{C}_m^H \bar{C}_m \hat{f}^{(n+1)}.$$

<div align="center">REFERENCES</div>

[1] C. V. Jakowatz, Jr., D. E. Wahl, P. H. Eichel, D. C. Ghiglia, and P. A. Thompson, *Spotlight-Mode Synthetic Aperture Radar: A Signal Processing Approach*. New York: Springer-Verlag, 1996.

[2] D. E. Wahl, P. H. Eichel, D. C. Ghiglia, and C. V. Jakowatz, Jr., "Phase gradient autofocus—A robust tool for high resolution SAR phase correction," *IEEE Trans. Aerosp. Electron.Syst.*, vol. 30, no. 3, pp. 827–835, Jul. 1994.

[3] L. Xi, L. Guosui, and J. Ni, "Autofocusing of ISAR images based on entropy minimization," *IEEE Trans. Aerosp. Electron. Syst.*, vol. 35, no. 4, pp. 1240–1252, Oct. 1999.

[4] J. R. Fienup, "Synthetic-aperture radar autofocus by maximizing sharpness," *Opt. Lett.*, vol. 25, no. 4, pp. 221–223, Feb. 2000.

[5] J. R. Fienup and J. J. Miller, "Aberration correction by maximizing generalized sharpness metrics," *J. Opt. Soc. Amer. A, Opt. Image Sci.*, vol. 20, no. 4, pp. 609–620, Apr. 2003.

[6] T. J. Kragh, "Monotonic iterative algorithm for minimum-entropy autofocus," in *Proc. ASAP*, Steamboat Springs, CO, 2006.

[7] R. L. Morrison, Jr., M. N. Do, and D. C. Munson, Jr., "SAR image autofocus by sharpness optimization: A theoretical study," *IEEE Trans. Image Process.*, vol. 16, no. 9, pp. 2309–2321, Sep. 2007.

[8] F. Berizzi and G. Corsini, "Autofocusing of inverse synthetic aperture radar images using contrast optimization," *IEEE Trans. Aerosp. Electron. Syst.*, vol. 32, no. 3, pp. 1185–1191, Jul. 1996.

[9] M. P. Hayes and S. A. Fortune, "Recursive phase estimation for image sharpening," presented at the Image Vision Computing New Zealand, Dunedin, New Zealand, 2005, unpublished.

[10] R. G. Paxman and J. C. Marron, "Aberration correction of speckled imagery with an image-sharpness criterion," *Proc. SPIE—Statistical Optics*, vol. 976, pp. 37–47, 1988.

[11] T. C. Calloway and G. Donohoe, "Subaperture autofocus for synthetic aperture radar," *IEEE Trans. Aerosp. Electron. Syst.*, vol. 30, no. 2, pp. 617–621, Apr. 1994.

[12] R. L. Morrison, Jr., M. N. Do, and D. C. Munson, Jr., "MCA: A multichannel approach to SAR autofocus," *IEEE Trans. Image Process.*, vol. 18, no. 4, pp. 840–853, Apr. 2009.

[13] W. D. Brown and D. C. Ghiglia, "Some methods for reducing propagation-induced phase errors in coherent imaging systems I: Formalism," *J. Opt. Soc. Amer. A, Opt. Image Sci.*, vol. 5, no. 6, pp. 924–941, Jun. 1988.

[14] D. C. Ghiglia and W. D. Brown, "Some methods for reducing propagation-induced phase errors in coherent imaging systems II: Numerical results," *J. Opt. Soc. Amer. A, Opt. Image Sci.*, vol. 5, no. 6, pp. 942–957, Jun. 1988.

[15] C. V. Jakowatz, Jr. and D. E. Wahl, "Eigenvector method for maximum-likelihood estimation of phase errors in synthetic aperture radar imagery," *J. Opt. Soc. Amer. A, Opt. Image Sci.*, vol. 10, no. 12, pp. 2539–2546, Dec. 1993.

[16] P. H. Eichel, D. C. Ghiglia, and C. V. Jakowatz, Jr., "Speckle processing method for synthetic aperture radar phase correction," *Opt. Lett.*, vol. 14, no. 1, pp. 1–3, Jan. 1989.

[17] L. Kuang-Hung, A. Wiesel, and D. C. Munson, Jr., "Synthetic aperture radar autofocus via semidefinite relaxation," in *Proc. IEEE Int. Conf. Acoust., Speech, Signal Process.*, 2010, pp. 1342–1345.

[18] W. G. Carrara, R. M. Majewski, and R. S. Goodman, *Spotlight Synthetic Aperture Radar: Signal Processing Algorithms*. Norwood, MA: Artech House, 1995.

[19] J. Walker, "Range-doppler imaging of rotating objects," *IEEE Trans. Aerosp. Electron. Syst.*, vol. AES-16, no. 1, pp. 23–52, Jan. 1980.

[20] M. Çetin and W. C. Karl, "Feature-enhanced synthetic aperture radar image formation based on nonquadratic regularization," *IEEE Trans. Image Process.*, vol. 10, no. 4, pp. 623–631, Apr. 2001.

[21] J. W. Burns, N. S. Subotic, and D. Pandelis, "Adaptive decomposition in electromagnetics," in *Proc. Int. Symp. Antennas Propag. Soc.*, 1997, pp. 1984–1987.

[22] T. J. Kragh and A. A. Kharbouch, "Monotonic iterative algorithms for sar image restoration," in *Proc. IEEE Int. Conf. Image Process.*, 2006, pp. 645–648.

[23] D. W. Warner, D. Ghiglia, A. FitzGerrell, and J. Beaver, "Two-dimensional phase gradient autofocus," in *Proc. SPIE—Image Reconstruction From Incomplete Data*, 2000, vol. 4123, pp. 162–173.

[24] L. C. Potter, E. Ertin, J. T. Parker, and M. Çetin, "Sparsity and compressed sensing in radar imaging," *Proc. IEEE*, vol. 98, no. 6, pp. 1006–1020, Jun. 2010.

[25] V. M. Patel, G. R. Easley, D. M. Healy, and R. Chellappa, "Compressed synthetic aperture radar," *IEEE J. Sel. Topics Signal Process.*, vol. 4, no. 2, pp. 244–254, Apr. 2010.

[26] R. Baraniuk and P. Steeghs, "Compressive radar imaging," in *Proc. IEEE Radar Conf.*, 2007, pp. 128–133.

[27] C. Gurbuz, J. McClellan, and R. Scott, Jr., "A compressive sensing data acquisition and imaging method for stepped frequency GPRs," *IEEE Trans. Signal Process.*, vol. 57, no. 7, pp. 2640–2650, Jul. 2009.

[28] I. Stojanovic, W. C. Karl, and M. Çetin, "Compressed sensing of monostatic and multi-static SAR," *Proc. SPIE—Algorithms Synthetic Aperture Radar Imagery XVI*, p. 733 705, 2009.

[29] C. Berger, S. Zhou, and P. Willett, "Signal extraction using compressed sensing for passive radar with OFDM signals," in *Proc. 11th Int. Conf. Inf. Fusion*, 2008, p. 16.

[30] I. Stojanovic and W. C. Karl, "Imaging of moving targets with multi-static SAR using an overcomplete dictionary," *IEEE J. Sel. Topics Signal Process.*, vol. 4, no. 1, pp. 164–176, Feb. 2010.

[31] M. Çetin and A. Lanterman, "Region-enhanced passive radar imaging," *Proc. Inst. Elect. Eng.—Radar Sonar Navig.*, vol. 152, no. 3, pp. 185–194, Jun. 2005.

[32] M. A. Herman and T. Strohmer, "High-resolution radar via compressed sensing," *IEEE Trans. Signal Process.*, vol. 57, no. 6, pp. 2275–2284, Jun. 2009.

[33] K. R. Varshney, M. Çetin, J. W. Fisher, III, and A. S. Willsky, "Sparse signal representation in structured dictionaries with application to synthetic aperture radar," *IEEE Trans. Signal Process.*, vol. 56, no. 8, pp. 3548–3561, Aug. 2008.

[34] C. D. Austin and R. L. Moses, "Wide-angle sparse 3-D synthetic aperture radar imaging for nonlinear flight paths," in *Proc. IEEE Nat. Aerosp. Electron. Conf.*, 2008, pp. 330–336.

[35] C. Austin, E. Ertin, and R. L. Moses, "Sparse multipass 3D imaging: Applications to the GOTCHA data set," in *Proc. SPIE—Defense Security Symp. Algorithms Synthetic Aperture Radar Imagery XVI*, 2009, vol. 7337, pp. 733 703-1–733703-12.

[36] M. Ferrara, J. Jackson, and M. Stuff, "Three-dimensional sparse-aperture moving-target imaging," in *Proc. SPIE—Algorithms Synthetic Aperture Radar Imagery XIV*, 2008, vol. 6970, p. 697 006.

[37] M. Herman and T. Strohmer, "General deviants: An analysis of perturbations in compressed sensing," *IEEE J. Sel. Topics Signal Process. —Special Issue Compressive Sensing*, vol. 4, no. 2, pp. 342–349, Apr. 2010.

[38] M. Çetin, W. C. Karl, and A. S. Willsky, "Feature-preserving regularization method for complex-valued inverse problems with application to coherent imaging," *Opt. Eng.*, vol. 45, no. 1, p. 017003, Jan. 2006.

[39] N. Ö. Önhon and M. Çetin, "A nonquadratic regularization based technique for joint SAR imaging and model error correction," in *Proc. SPIE—Algorithms for Synthetic Aperture Radar Imagery XVI*, 2009, vol. 7337, pp. 73370C-1–73370C-10.

[40] N. Ö. Önhon and M. Çetin, "Joint sparsity-driven inversion and model error correction for radar imaging," in *IEEE Int. Conf. Acoust., Speech, Signal Process.*, 2010, pp. 1206–1209.

[41] MSTAR, Air Force Res. Lab., Sensor Data Management System [Online]. Available: https://www.sdms.afrl.af.mil /index.php?collection=mstar

[42] Backhoe Data Sample & Visual-D Challenge Problem, Air Force Research Laboratory, Sensor Data Management System [Online]. Available: https://www.sdms.afrl.af.mil

[43] M. Çetin and R. L. Moses, "SAR imaging from partial-aperture data with frequency-band omissions," in *Proc. SPIE—Algorithms for Synthetic Aperture Radar Imagery XII*, 2005, vol. 5808, pp. 32–43.

N. Özben Önhon (S'09) received the B.S. degree in electronics and telecommunication engineering and the M.S. degree in telecommunication engineering from Istanbul Technical University, Istanbul, Turkey, in 2003 and 2006, respectively. She is currently working toward the Ph.D. degree from Sabancı University, Istanbul.

Her research interests include signal and image processing.

Müjdat Çetin (S'98–M'02) received the Ph.D. degree in electrical engineering from Boston University, Boston, MA, in 2001.

From 2001 to 2005, he was with the Laboratory for Information and Decision Systems, Massachusetts Institute of Technology, Cambridge. Since September 2005, he has been a faculty member with Sabancı University, Istanbul, Turkey. His research interests include statistical signal and image processing, inverse problems, radar imaging, brain–computer interfaces, machine learning, computer vision, data fusion, wireless sensor networks, biomedical information processing, and sensor array signal processing.

Dr. Çetin has served as the Technical Program Cochair for the 2010 International Conference on Pattern Recognition and for the 2006 IEEE Turkish Conference on Signal Processing, Communications, and their Applications. He is currently an Area Editor for the *Journal of Advances in Information Fusion*, a Guest Editor for *Pattern Recognition Letters*, and a EURASIP Liaison Officer for Turkey. He was the recipient of several awards including the 2010 IEEE Signal Processing Society Best Paper Award, the 2010 METU Parlar Foundation Research Incentive Award, the 2008 Turkish Academy of Sciences Distinguished Young Scientist Award, the 2007 Elsevier Signal Processing Journal Best Paper Award, and the 2006 TÜBİTAK Career Award.